Title:
Greener green and bluer blue: Ocean Poleward Greening Over the Past Two Decades

Authors:

Haipeng Zhao[1], M. Susan Lozier[2]*, Manfredi Manizza[3], Nicolas Cassar[1]*

Affiliations:

[1]Division of Earth and Climate Sciences, Nicholas School of the Environment, Duke University; Durham, NC, 27708, USA.

[2] School of Earth and Atmospheric Sciences, Georgia Institute of Technology; Atlanta, GA, 30332, USA.

[3] Geosciences Research Division, Scripps Institution of Oceanography, University of California; San Diego, La Jolla, CA, 92093, USA.

*Corresponding author. Email: Nicolas.Cassar@duke.edu; susan.lozier@gatech.edu

Abstract: While the global greening associated with climate change is well documented on land, similar trends in the ocean have not been thoroughly identified. Using satellite observations of ocean chlorophyll *a* (Chl) concentration, we show that the surface ocean experienced a poleward greening from 2003 to 2022. Contemporaneously, the subtropical regions of the northern hemisphere experienced a decrease in Chl. As such, the latitudinal disparity in Chl, as documented by an inequality index, has been increasing over the past two decades, particularly in the northern hemisphere. Rising water temperatures may primarily influence the Chl trends. The increasing Chl inequality—marked by "greener green and bluer blue" waters—has the potential to cascade to higher trophic levels with implications for the fisheries and economies of coastal nations.

Main Text: Earth greening refers to an increasing trend in global leaf area, an indication of enhanced photosynthetic activity on land. Numerous studies since the 1990s have reported this phenomenon across high-latitude, temperate, and tropical regions, and have attributed it to climate and land use change (*1–4*). In 2023, nearly 63% of global vegetated areas exhibited positive normalized difference vegetation index (NDVI) anomalies, the third highest record since 2000, indicating a continuous increase in terrestrial greenness (*5*). Given that the ocean contributes to about half of the Earth's primary production, a similar analysis of trends in global ocean photosynthesis in response to climate change is critical, yet remains elusive.

Observing secular trends in the ocean has been challenging due to the strong natural variability in marine ecosystems (*6–9*). As on land, photosynthesis in the marine environment is influenced by several factors including light availability, temperature, and nutrient supply. However, the impact of these factors in the ocean is complicated by its fluidity: phytoplankton, which are the primary photosynthesizers in the ocean, can be mixed into or away from the photic zone and/or experience sharp temperature changes due to advection. The nutrient supply is similarly affected. Upwelling and downwelling driven by large-scale winds, as well as local mixing and advection, place strong constraints on the nutrient supply to the surface waters. This complexity hinders a simple projection as to how marine photosynthesis will respond to a warming world.

Driven by the broad pattern of wind-driven upwelling and downwelling, the spatial distribution of nutrients in the ocean is largely characterized by latitudinal differences (*10*, *11*). As such, we focus on the identification of latitudinal trends in chlorophyll *a* (Chl) concentration (a metric for phytoplankton biomass), a choice also intended to reduce the signal-to-noise ratio in our trend estimates. We aim to elucidate whether regional changes reported elsewhere (*12–15*) are reflective of a broader global redistribution in Chl. To that end, we use the 20-year record of Chl from the Moderate Resolution Imaging Spectroradiometer (MODIS) aboard the Aqua satellite (hereafter referred to as MODIS-Aqua). MODIS-Aqua began collecting data in July 2002 and stands as the longest-serving solitary sensor in operation. The latest 2022 Reprocessing version (R2022) released by NASA, which includes instrument calibration updates that address degradation issues, now provides a stable data source for the past two decades. Challenges arise from the inherent characteristics of the Chl product, including a low signal-to-noise ratio and gaps in observations. To mitigate these issues, we first interpolate the Chl data using an algorithm that has recently been shown to improve the time series of global Chl in the open ocean. We then spatially aggregate the data averaging measurements over latitudinal bands to detect underlying large-scale trends (Methods).

We start by showing the well-known and distinctive spatial distribution of climatological Chl (Fig. 1a, b). The elevated Chl (mean of 0.38 mg m^{-3}) in the subpolar regions (40 – 60°) stands in sharp contrast to the relatively low Chl (mean of 0.074 mg m^{-3}) in the oligotrophic gyres of the mid-latitudes (10 – 30°). In the tropics (0 – 10°), characterized by strong upwelling that boosts phytoplankton growth, the mean Chl is again elevated (mean of 0.14 mg m^{-3}). To explore latitudinal trends, we calculate the annual mean Chl of each 2° latitudinal band between 60°S – 80°N from 2003 to 2022 and then use the Sen's slope estimator to determine trends (Methods). We find that Chl has significantly decreased at an average rate of 0.55% yr^{-1} in the northern subtropical region (20 – 40°N) (Fig 1c). In contrast, Chl shows increasing trends in both northern and southern subpolar regions at a rate of 0.28% yr^{-1} and 0.44% yr^{-1}, respectively. Moreover, consistent with previous studies (*16*, *17*), we find that the Arctic Ocean (66 – 80°N) has experienced a significant increase in Chl at a rate of 1.99% yr^{-1}. Collectively these results

indicate a broad pattern whereby Chl is decreasing in the low Chl waters of the subtropical and tropical regions while increasing in the high Chl waters at higher latitudes (>40°).

To assess the relative contribution of these latitudinal bands to the total Chl in each hemisphere we use a Lorenz curve and the corresponding Gini index, which were originally developed for economic analysis (Methods). We examine the Northern Hemisphere (NH) and Southern Hemisphere (SH) separately because of the well-known differences in the dynamics that govern the high latitudes in these hemispheres. Given the unique environmental conditions in the Arctic Ocean and previous work in this region, we hereafter focus on analyzing the open ocean between 60°S and 60°N (see the study (*16*) for Arctic-specific trends). As seen by the Lorenz curve, in which the 30 latitudinal bands are ranked in ascending order according to their contribution to the cumulative chlorophyll in each hemisphere, the subpolar latitudes (40 – 60°N) place in the top 10 latitudinal bands in the NH (Fig. 2a), contributing 55.6% to the total. In contrast, the latitudinal bands between 20 – 30°N fall in the 20th percentile, contributing only 8.1%. In the SH, the latitudinal bands with the largest contribution (28.3%) to the cumulative total are between 40 – 50°S. They are followed by latitudes between 30 – 40°S (18.8%), between 50 – 60°S (18.2%), and 0 – 10°S (15.9%) (Fig. 2c). As seen here, the NH has a greater latitudinal disparity than the SH mainly because Chl in the NH subpolar region exceeds that in the comparable SH region. This difference is likely mainly attributable to the known iron deficiency that limits phytoplankton biomass (*18*) in the high nutrient-low chlorophyll Southern Ocean.

From the Lorenz curve, we next calculate trends in the Gini index of area-integrated Chl over each latitudinal band from 2003 to 2022 for each hemisphere (Methods, similar trends are observed with latitudinal averaged Chl, see fig.S1). We find a growing latitudinal disparity in Chl in the NH, as measured by a significant increase of 0.20% yr^{-1}in the Gini index. The significant increase of the Gini index tends to occur in winter and autumn seasons (fig. S2), indicating a seasonal difference in the latitudinal disparity of Chl. In the SH, the increase is not statistically significant (despite an increase in Chl concentrations in the SH subpolar latitudes). One reason for this difference is that Chl has decreased significantly in the northern subtropical regions where the relatively low Chl has become lower over the same period, whereas no such trends are detected in the SH. We note that our latitudinal binning masks a myriad of variability in Chl trends at regional and biome scales, with spatial heterogeneity in the magnitude and sign of linear trends, particularly in the southern subtropical regions. While a local analysis is beyond the scope of our study, contrasting trends at the local level likely explain the absence of trends in certain latitudinal bands (e.g. SH subtropics). For further context, a comparison with recent literature on global ocean color trends that focus on region is provided in the supplementary material (Table S1).

As a first approximation, we examine the trends of four environmental factors (Fig. 3) believed to critically influence Chl concentrations: sea surface temperature (SST), mixed layer depth (MLD), photosynthetically available radiation (PAR), and wind speed (WS), and then determine the observed sensitivity of Chl to these factors. A few patterns stand out from the comparison of trends. In the northern subpolar regions (40 – 60°N), where significant increases in Chl are primarily detected from October to February at a rate of 0.88 ± 0.41% yr^{-1} (Fig. 3a), we note concurrent increases in SST and PAR (Fig. 3b, d), as well as a shoaling in the MLD (Fig. 3c). In the northern subtropical region (20 – 40°N), where Chl shows a year-round decreasing trend at a rate of -0.75 ±0.25% yr^{-1}, with significant changes observed in 56.7% of the region (Fig. 3a), SST shows significant increases throughout the year in 79.2% of the grids (Fig. 3b). Finally, in the southern subpolar regions (40 – 60°S), where Chl has increased significantly in the months of

April to August at a rate of 1.24 ± 0.64% yr^{-1}, a few concurrent SST trends are also observed (Fig. 3a, b).

The observed sensitivity of Chl trends to trends in the four environmental variables suggests that SST is a dominant factor for Chl changes in the subpolar region of both hemispheres and in the subtropics of the northern hemisphere (Fig. 4). The increase in Chl in the subpolar regions is likely associated with the observed increase in autumn and winter blooms (*19*, *20*), consistent with projected increases in NPP driven by sea ice retreat, shoaling of mixed layers, and a reduction in light limitation (*16*, *21*, *22*), all tightly linked to the surface warming observed here. In the northern hemisphere subtropics, the decreasing Chl trend and concurrent increasing SST trend are supported by in situ observations at the Bermuda Atlantic Time-series site (BATS). Previous study (*23*) found that rising SST reduces phytoplankton productivity in the oligotrophic ocean, putatively through a reduction in nutrient supply, a result consistent with increased stratification observed in recent years (*24*). The southern hemisphere subtropics do not exhibit a clear sensitivity to any of the variables, likely because the Chl trends here are the weakest across all latitudes (Fig. 3a). Finally, the lack of significant trends in the tropics for all environmental variables (Fig. 3b–e) precludes any attribution of the decreasing Chl trend observed there (Fig. 4).

As mentioned above, complex dynamics in the ocean environment complicate the attribution of Chl changes. While our analysis suggests that broad scale SST changes are likely driving latitudinal Chl changes, our results are inconclusive for the three other variables studied here. Regional studies provide additional insights to this global analysis. For example, wind speed emerges as a significant factor in annual Chl variation across both tropical regions and eastern boundary currents (*25*, *26*). In the tropical Indian Ocean, reduced wind speeds have been correlated with increased stratification, which suppresses nutrient upwelling, thus contributing to declining Chl. Conversely, in the California Current System, elevated wind speeds have been found to facilitate upwelling, thus enhancing phytoplankton biomass and fostering a "greening" effect. Modeling studies that incorporate these variables, and others such as turbulent mixing and aerosol deposition (*7*, *8*), are needed to further elucidate the mechanisms driving the latitudinal Chl trends observed here.

It remains to be established whether the significant trends over the 20-year record reported here stem from natural variability over the satellite era or are driven by a changing climate. Previous studies suggest that satellite time series would need to be ~30 – 40 years in length to distinguish climate-driven Chl trends from internal variability (*12*, *27*, *28*). Because variations in Chl reflect both biomass and physiology (*6*), we cannot attribute the Chl trends changes in phytoplankton biomass. However, our observations of poleward greening and increasing latitudinal disparity align with 21st century projections of a sustained decrease in NPP in the low- and mid-latitudes that is coupled with an increase in high latitude areas (*29*, *30*). Through trophic amplification, the decline in phytoplankton biomass associated with climate warming will have a more pronounced impact on biomass at higher trophic levels (*31*, *32*, *33*) with a projected decline in fish production and fisheries in the tropics, and an increase in the high latitudes (*34*, *35*, *36*). More than 50% of the global fish catch comes from tropical and subtropical regions, with significant contributions from coastal fisheries. While our study focuses on open ocean waters, any persistent changes in these areas could profoundly impact low- and middle-income nations, such as Pacific Island Nations, that rely on fisheries for sustenance and economic development. (*38*, *39*). Future investigations should focus on these regions to provide a more comprehensive understanding. In particular, it will be important to investigate how climate change, and climate

mitigation through iron fertilization (*40*), could synergistically impact air-sea CO_2 fluxes, and exacerbate fisheries inequity.

References and Notes

1. R. B. Myneni, C. D. Keeling, C. J. Tucker, G. Asrar, R. R. Nemani, Increased plant growth in the northern high latitudes from 1981 to 1991. Nature 386, 698-702 (1997). https://doi.org:10.1038/386698a0
2. Z. Zhu et al., Greening of the Earth and its drivers. Nature Climate Change 6, 791-795 (2016). https://doi.org:10.1038/nclimate3004
3. C. Chen et al., China and India lead in greening of the world through land-use management. Nature Sustainability 2, 122-129 (2019). https://doi.org:10.1038/s41893-019-0220-7
4. S. Piao et al., Characteristics, drivers and feedbacks of global greening. Nature Reviews Earth & Environment 1, 14-27 (2020). https://doi.org:10.1038/s43017-019-0001-x
5. X. Li et al., Vegetation greenness in 2023. Nature Reviews Earth & Environment 5, 241-243 (2024). https://doi.org:10.1038/s43017-024-00543-z
6. M. J. Behrenfeld et al., Revaluating ocean warming impacts on global phytoplankton. Nature Climate Change 6, 323-330 (2016). https://doi.org:10.1038/nclimate2838
7. S. R. Brody, M. S. Lozier, Changes in dominant mixing length scales as a driver of subpolar phytoplankton bloom initiation in the North Atlantic. Geophysical Research Letters 41, 3197-3203 (2014). https://doi.org:https://doi.org/10.1002/2014GL059707
8. T. K. Westberry et al., Atmospheric nourishment of global ocean ecosystems. Science 380, 515-519 (2023). https://doi.org:doi:10.1126/science.abq5252
9. W. Tang et al., Widespread phytoplankton blooms triggered by 2019–2020 Australian wildfires. Nature 597, 370-375 (2021). https://doi.org:10.1038/s41586-021-03805-8
10. K. W. Bruland, R. Middag, M. C. Lohan, in Treatise on Geochemistry (Second Edition), H. D. Holland, K. K. Turekian, Eds. (Elsevier, Oxford, 2014), pp. 19-51.
11. S. Levitus, M. E. Conkright, J. L. Reid, R. G. Najjar, A. Mantyla, Distribution of nitrate, phosphate and silicate in the world oceans. Progress in Oceanography 31, 245-273 (1993). https://doi.org:https://doi.org/10.1016/0079-6611(93)90003-V
12. C. Beaulieu et al., Factors challenging our ability to detect long-term trends in ocean chlorophyll. Biogeosciences 10, 2711-2724 (2013). https://doi.org:10.5194/bg-10-2711-2013
13. M. L. Hammond, C. Beaulieu, S. K. Sahu, S. A. Henson, Assessing trends and uncertainties in satellite-era ocean chlorophyll using space-time modeling. Global Biogeochemical Cycles 31, 1103-1117 (2017). https://doi.org:https://doi.org/10.1002/2016GB005600
14. M. van Oostende, M. Hieronymi, H. Krasemann, B. Baschek, Global ocean colour trends in biogeochemical provinces. Frontiers in Marine Science 10, (2023). https://doi.org:10.3389/fmars.2023.1052166

15. S. Yu, Y. Bai, X. He, F. Gong, T. Li, A new merged dataset of global ocean chlorophyll-a concentration for better trend detection. Frontiers in Marine Science 10, (2023). https://doi.org:10.3389/fmars.2023.1051619

16. K. M. Lewis, G. L. van Dijken, K. R. Arrigo, Changes in phytoplankton concentration now drive increased Arctic Ocean primary production. Science 369, 198 (2020). https://doi.org:10.1126/science.aay8380

17. M. Ardyna, K. R. Arrigo, Phytoplankton dynamics in a changing Arctic Ocean. Nature Climate Change 10, 892-903 (2020). https://doi.org:10.1038/s41558-020-0905-y

18. J. H. Martin, R. M. Gordon, S. E. Fitzwater, Iron in Antarctic waters. Nature 345, 156-158 (1990). https://doi.org:10.1038/345156a0

19. H. Zhao, A. Matsuoka, M. Manizza, A. Winter, Recent Changes of Phytoplankton Bloom Phenology in the Northern High-Latitude Oceans (2003–2020). Journal of Geophysical Research: Oceans 127, e2021JC018346 (2022). https://doi.org:https://doi.org/10.1029/2021JC018346

20. S. J. Thomalla, S.-A. Nicholson, T. J. Ryan-Keogh, M. E. Smith, Widespread changes in Southern Ocean phytoplankton blooms linked to climate drivers. Nature Climate Change, (2023). https://doi.org:10.1038/s41558-023-01768-4

21. L. Bopp et al., Multiple stressors of ocean ecosystems in the 21st century: projections with CMIP5 models. Biogeosciences 10, 6225-6245 (2013). https://doi.org:10.5194/bg-10-6225-2013

22. S. McClish, S. M. Bushinsky, Majority of Southern Ocean Seasonal Sea Ice Zone Bloom Net Community Production Precedes Total Ice Retreat. Geophysical Research Letters 50, e2023GL103459 (2023). https://doi.org:https://doi.org/10.1029/2023GL103459

23. D. D'Alelio et al., Machine learning identifies a strong association between warming and reduced primary productivity in an oligotrophic ocean gyre. Scientific Reports 10, 3287 (2020). https://doi.org:10.1038/s41598-020-59989-y

24. J.-B. Sallée et al., Summertime increases in upper-ocean stratification and mixed-layer depth. Nature 591, 592-598 (2021). https://doi.org:10.1038/s41586-021-03303-x

25. M. K. Roxy et al., A reduction in marine primary productivity driven by rapid warming over the tropical Indian Ocean. *Geophysical Research Letters* **43**, 826-833 (2016).

26. M. Kahru, Z. Lee, R. M. Kudela, M. Manzano-Sarabia, B. Greg Mitchell, Multi-satellite time series of inherent optical properties in the California Current. *Deep Sea Research Part II: Topical Studies in Oceanography* **112**, 91-106 (2015).

27. S. A. Henson et al., Detection of anthropogenic climate change in satellite records of ocean chlorophyll and productivity. Biogeosciences 7, 621-640 (2010). https://doi.org:10.5194/bg-7-621-2010

28. S. Dutkiewicz et al., Ocean colour signature of climate change. Nature Communications 10, 578 (2019). https://doi.org:10.1038/s41467-019-08457-x

29. M. Steinacher et al., Projected 21st century decrease in marine productivity: a multi-model analysis. Biogeosciences 7, 979-1005 (2010). https://doi.org:10.5194/bg-7-979-2010

30. L. Kwiatkowski et al., Twenty-first century ocean warming, acidification, deoxygenation, and upper-ocean nutrient and primary production decline from CMIP6 model projections. Biogeosciences 17, 3439-3470 (2020). https://doi.org:10.5194/bg-17-3439-2020

31. H. K. Lotze et al., Global ensemble projections reveal trophic amplification of ocean biomass declines with climate change. Proceedings of the National Academy of Sciences 116, 12907-12912 (2019). https://doi.org:doi:10.1073/pnas.1900194116

32. A. Atkinson et al., Steeper size spectra with decreasing phytoplankton biomass indicate strong trophic amplification and future fish declines. Nature Communications 15, 381 (2024). https://doi.org:10.1038/s41467-023-44406-5

33. L. Russo et al., Long-term oscillations in the normalized biomass-size spectrum reveal the impact of oligotrophication on zooplankton trophic structure in the North Atlantic Subtropical Gyre. Marine Environmental Research 193, 106295 (2024).

34. J. L. Blanchard et al., Potential consequences of climate change for primary production and fish production in large marine ecosystems. Philosophical Transactions of the Royal Society B: Biological Sciences 367, 2979-2989 (2012). https://doi.org:doi:10.1098/rstb.2012.0231

35. W. W. L. CHEUNG et al., Large-scale redistribution of maximum fisheries catch potential in the global ocean under climate change. Global Change Biology 16, 24-35 (2010). https://doi.org:https://doi.org/10.1111/j.1365-2486.2009.01995.x

36. V. W. Y. Lam, W. W. L. Cheung, U. R. Sumaila, Marine capture fisheries in the Arctic: winners or losers under climate change and ocean acidification? Fish and Fisheries 17, 335-357 (2016). https://doi.org:https://doi.org/10.1111/faf.12106

37. D. Pauly, D. Zeller, & M. L. D Palomares, Sea Around Us Concepts, Design and Data. Sea around us http://www.seaaroundus.org (2020).

38 U. R. Sumaila, W. W. L. Cheung, V. W. Y. Lam, D. Pauly, S. Herrick, Climate change impacts on the biophysics and economics of world fisheries. Nature Climate Change 1, 449-456 (2011). https://doi.org:10.1038/nclimate1301

39 V. W. Y. Lam et al., Climate change, tropical fisheries and prospects for sustainable development. Nature Reviews Earth & Environment 1, 440-454 (2020). https://doi.org:10.1038/s43017-020-0071-9

40 A. Tagliabue et al., Ocean iron fertilization may amplify climate change pressures on marine animal biomass for limited climate benefit. Global Change Biology 29, 5250-5260 (2023). https://doi.org:https://doi.org/10.1111/gcb.16854

41 E. Pauthenet *et al.*, Contrasted Trends in Chlorophyll-a Satellite Products. *Geophysical Research Letters* **51**, e2024GL108916 (2024).

42 H. Zhao, A. Matsuoka, M. Manizza, A. Winter, DINEOF Interpolation of Global Ocean Color Data: Error Analysis and Masking. *Journal of Atmospheric and Oceanic Technology* **41**, 953-968 (2024).

43 A. R. Fay, G. A. McKinley, Global open-ocean biomes: mean and temporal variability. Earth System Science Data 6, 273-284 (2014).

44 J. d. Kloe, A. Stoffelen, A. Verhoef, Improved Use of Scatterometer Measurements by Using Stress-Equivalent Reference Winds. IEEE Journal of Selected Topics in Applied Earth Observations and Remote Sensing 10, 2340-2347 (2017). https://doi.org:10.1109/JSTARS.2017.2685242

45 D. Carroll, et al., The ECCO-Darwin Data-Assimilative Global Ocean Biogeochemistry Model: Estimates of Seasonal to Multidecadal Surface Ocean pCO2 and Air-Sea CO2 Flux. Journal of Advances in Modeling Earth Systems 12, e2019MS001888 (2020). https://doi.org:https://doi.org/10.1029/2019MS001888

46 G. G. Katul *et al.*, On the spectrum of soil moisture from hourly to interannual scales. *Water Resources Research* **43**, (2007).

47 T. Zhou, C. Ni, M. Zhang, P. Xia, Assessing Spatial and Temporal Distribution of Algal Blooms Using Gini Coefficient and Lorenz Asymmetry Coefficient. *Frontiers in Environmental Science* **10**, (2022).

48 P. K. Sen, Estimates of the Regression Coefficient Based on Kendall's Tau. Journal of the American Statistical Association 63, 1379-1389 (1968). https://doi.org:10.1080/01621459.1968.10480934

49 M. Collaud Coen et al., Effects of the prewhitening method, the time granularity, and the time segmentation on the Mann–Kendall trend detection and the associated Sen's slope. Atmos. Meas. Tech. 13, 6945-6964 (2020).

50 D. M. Hamby, A review of techniques for parameter sensitivity analysis of environmental models. Environmental Monitoring and Assessment 32, 135-154 (1994). https://doi.org:10.1007/BF00547132

Acknowledgments: We thank Dr. Kevin Arrigo and Dr. Gert Van Djiken for sharing the Arctic dataset on chlorophyll concentration. MSL and NC acknowledge support from the U.S. National Science Foundation (OCE-1948335, OCE-2123198). M.M. acknowledges support from NASA (IDS-#19-0113) and NSF (OPP-192292 and OCE-2049294).

Funding:

U.S. National Science Foundation OCE-1948335

U.S. National Science Foundation OCE-2123198

Author contributions:

Conceptualization: HZ, MSL, NC

Methodology: HZ

Investigation: HZ

Visualization: HZ

Funding acquisition: MSL, NC

Project administration: HZ, MSL, NC

Supervision: MSL, NC

Writing – original draft: HZ

Writing – review & editing: HZ, MSL, NC

Data curation: MM

Competing interests: Authors declare that they have no competing interests.

Data and materials availability: Daily 4-km standard MODIS-Aqua datasets on Chl, SST and PAR are available from https://oceancolor.gsfc.nasa.gov/l3/. Monthly 0.125-degree sea surface wind speed are available from https://data.marine.copernicus.eu/product/WIND_GLO_PHY_L4_MY_012_006/services. DINEOF+ code is available from https://github.com/zhprm1992/DINEOF-plus.git

Supplementary Materials

Materials and Methods

Satellite Chl observation

We obtained level-3, daily, 4 km-binned Chl data derived from MODIS-Aqua from the ocean color website (https://oceancolor.gsfc.nasa.gov/) for the period of Jan 1, 2003 to Dec 31, 2022. NASA has reprocessed all ocean color products several times during the mission's operation to account for MODIS-Aqua degradation issues. The current version is R2022, in which the sensor drift issue has been corrected to the end of 2022 (https://oceancolor.gsfc.nasa.gov/data/reprocessing/r2022/noaa20/). Compared to previous versions, R2022 shows a significant change in the MODIS-Aqua time series Chl, with a decrease on the order of 10 – 20% for the recent 5 years (https://oceancolor.gsfc.nasa.gov/data/reprocessing/r2022/aqua/). By the time we submitted the article, multi-sensor datasets such as OC-CCI 6.0 had not incorporated NASA R2022 products (CMEMS-OC-QUID-009-107to108), thereby reducing the accuracy of Chl trends. Furthermore, recent studies have revealed possible biases in detecting Chl trends using multi-sensor products due to the inconsistencies between missions (*13, 41*). North of 65ºN, we use the dataset of Lewis, et al. (*16*). This dataset has been produced using a modified version of the standard empirical algorithm (AO.emp). It is developed by using coincident measurements of *in situ* and remote sensing reflectance in order to account for the unique bio-optical properties of the Arctic Ocean.

DINEOF+

We aggregated Chl values by spatially averaging over 2 degree grids and then applying DINEOF+ to interpolate data gaps in the open ocean. DINEOF+ is a variant of learning algorithms that uses singular value decomposition (SVD) to address missing data. It has recently been shown to be an effective interpolation method to increase data coverage of global Chl observations. The reconstructed Chl time series also demonstrates a higher correlation to *in situ* observations compared to the original product (*42*). The boundary for the open ocean is based on climatological criteria developed by Fay and McKinley (*43*), who classified 17 open-ocean biomes according to observations of Chl, SST, and MLD. This boundary excludes coastal regions characterized by high Chl variance and complex water constituents due to strong upwelling and land influence. This choice also reduces the impact of high Chl variance on DINEOF+ performance as well as the influence of known biases in ocean color data for Case 2 waters. Using the reconstructed daily Chl, we generated a 20-year time series of monthly and annual Chl concentrations.

Datasets on ocean surface conditions: temperature, PAR, wind, and mixed layer depth

Monthly average datasets of SST, PAR, wind, and mixed layer depth were analyzed for the period Jan 2003 – Dec 2022: (1) SST and PAR: MODIS-Aqua level-3 bin datasets at 4 km

spatial resolution from NASA's ocean color website. (2) Sea surface wind: ECMWF ERA5 based level-4 at 0.25 degree spatial resolution from Copernicus Marine Service (https://marine.copernicus.eu/). Bias corrections are performed by using scatterometer observations from satellites (*44*). (3) MLD: 0.25 degree spatial resolution derived from the ECCO-Darwin model (*45*). All datasets are spatially averaged to a 2-degree grid, then averaged to latitudinal bands.

Lorenz curve and Gini index

The Lorenz curve is commonly used in economics to visually illustrate the distribution of income or wealth within a society. It plots the cumulative percentage of total income received by the cumulative percentage of population. In this study, we take the sea surface area-integrated Chl concentration of each latitudinal band as a discrete unit and plot the cumulative Chl (x%) against the cumulative number of latitudinal bands (y%) by the ascending order of Chl level from lowest to highest. The resulting plot shows the inequality of Chl distribution among latitudinal bands (Fig. 2a, c).

The Gini index is a metric that summarizes the level of inequality represented by the Lorenz curve. It has previously been used to evaluate the unevenness of distributions, including soil moisture and phytoplankton blooms in a large lake (*46 47*). We calculate the Gini index (G) to quantify the disparity level of Chl in both hemispheres.

The classic definition of G is:

$$G = \frac{\sum_{i=1}^{n}\sum_{j=1}^{n}|x_i - x_j|}{2n^2\bar{x}} \quad (1)$$

where x_i is the average value of Chl concentration of the *i*th latitude band, n is the number of latitudinal bands and i is the rank of values in ascending order. When x values are placed in ascending order, the formulation is:

$$G = \frac{\sum_{i=1}^{n}(2i - n - 1)x_i}{n\sum_{i=1}^{n}x_i} \quad (2)$$

G ranges between 0, where there is perfect equality in the latitudinal distribution of global Chl, and 1, where Chl is concentrated in a single latitudinal band.

Statistical analysis

We use the Man-Kendall (MK) test with Sen's slope method (*48*) to detect the trend in annual Chl of each latitudinal band and to estimate the slope β. The Sen's estimator is a nonparametric method that uses the median slope of all lines through sample points (Eq. 3).

$$\beta = median\left(\frac{x_i - x_j}{t_i - t_j}\right) \quad (3)$$

where $t_1 < t_2 \cdots < t_{20}$, x_i and x_j are observed values at times t_i and t_j respectively, $1 \le i < j \le 20$.

Alternatively, β may be estimated by using least square regression. However, the trend detected in this way is sensitive to outliers. In addition, it has been noted that Chl time series are not normally distributed with constant variance over the global ocean (*12*). Compared to the linear

regression method, the Sen's estimator of slope is less sensitive to outliers and provides an exact confidence interval without assuming normality and constant variance. To correct for serial autocorrelation in the MK test's statistical significance, we apply the modified MK test to data of significant autocorrelation at 95% confidence limit. This approach developed by Hamed and Rao is effective for data with arbitrary autocorrelation structure by modifying the variance of the MK statistic (*49*).

We define the observed sensitivity as the ratio of Chl trend slope to the trend slope of the driving factor under consideration (i.e., SST, MLD, PAR or WS), multiplied by the ratio of the 2003 annual means of driving factors (DF) and Chl (Eq. 4). Doing so allows us to compare the changing rate of Chl relative to different driving factors (*50*). We use:

$$\alpha_i = \frac{\beta_{Chl}}{\beta_{DF_i}} \times \frac{\overline{DF_{2003}}}{\overline{Chl_{2003}}} \quad (4)$$

where overlines indicate annual mean. α_i is the standardized observed sensitivity of Chl trend to trend of the driving factor. β_{Chl} , β_{DF_i} are the estimated slopes of the trends in Chl and the driving factor DF_i (i.e., SST, MLD, PAR, and WS), respectively. Only significant trends ($p < 0.05$) are used for calculating the observed sensitivity. We note that the observed sensitivity is statistical and does not necessarily reflect causation.

Figs. S1 to S2

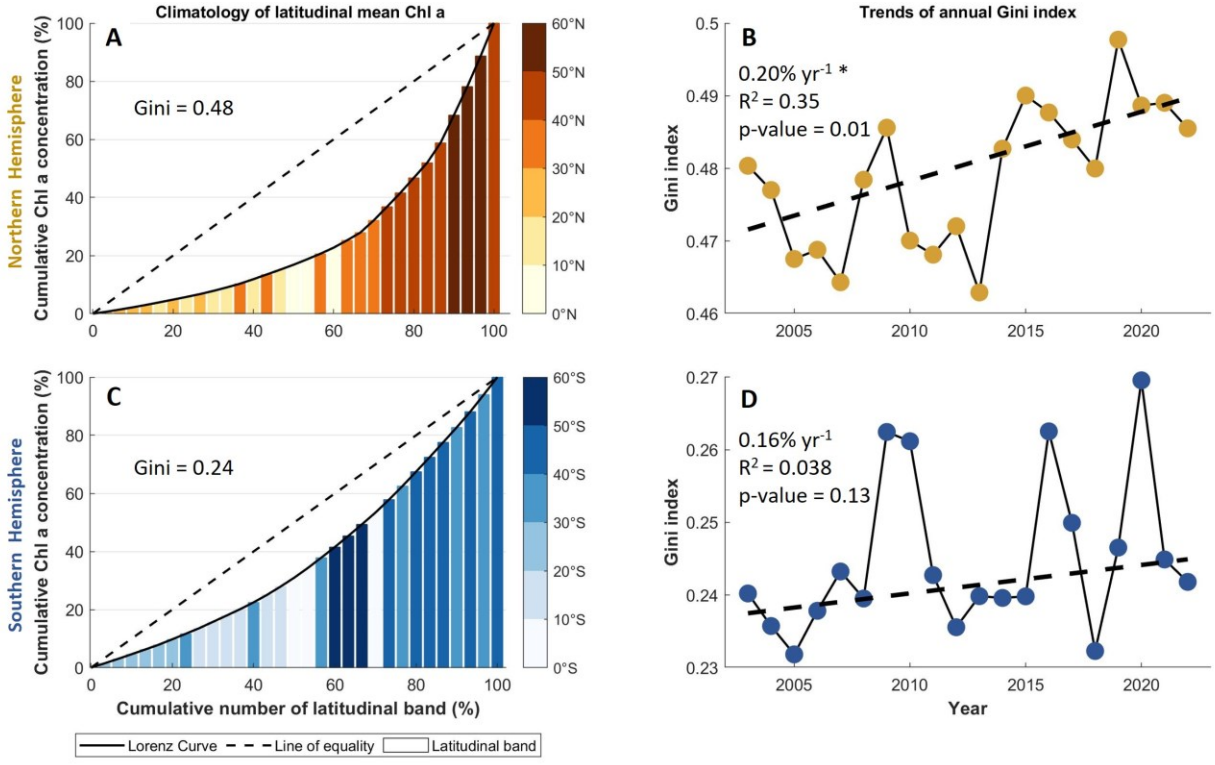

fig. S1 Latitudinal disparity in Chl concentration. (**A**, **C**) Lorenz curves of climatological Chl concentration of 2° latitudinal bands in the Northern (0 – 60°N) and Southern Hemispheres (0 – 60°S). Bars represent the cumulative latitudinal mean Chl concentration, ordered in ascending

averaged Chl concentration. (**B**, **D**) Interannual variability of the Gini index during the 2003 – 2022 period with significant trends ($p < 0.05$) indicated by an asterisk.

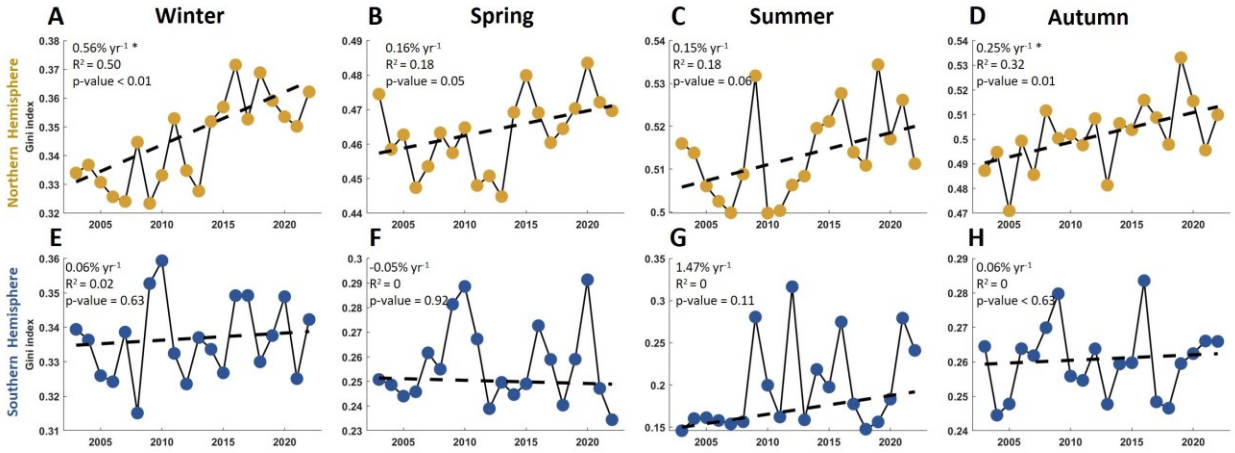

fig. S2 Long-term trends in the Gini index in seasons. (**A**–**D**) Northern Hemisphere (0 – 60°N). (**E**–**H**) Southern Hemisphere. Dots represent the annual Gini index of latitudinal and season- averaged Chl concentration. Dashed line displays the annual Sen's slope with Mann-Kendall (MK) test significance (* $p < 0.05$)

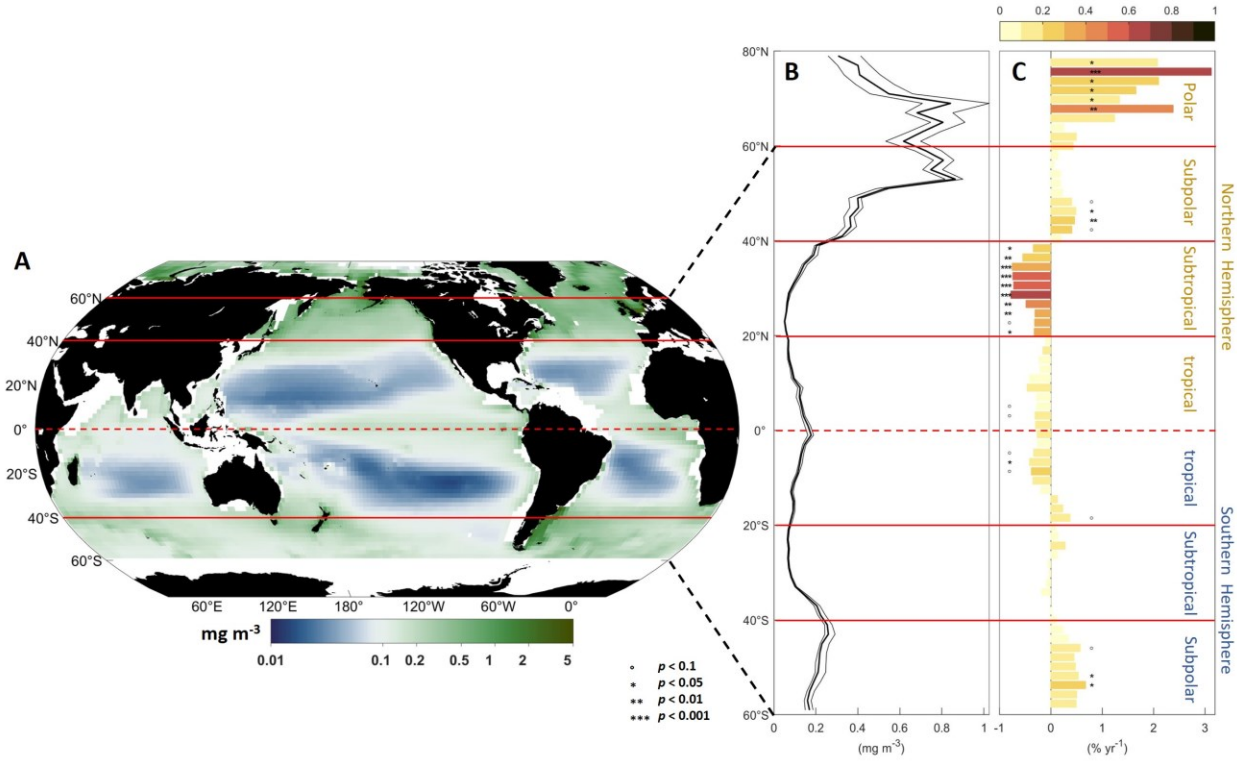

Fig. 1. Global distribution and latitudinal trends of surface Chl at 2° resolution. (**A**) Climatological mean Chl between 60S – 60N (2003 – 2022), and north of 60°N (2003 – 2020).

Coastal regions and areas south of 60°S are excluded. (**B**) Median of the climatological Chl (thick line) and the 10th and 90th percentiles (thin lines) as a function of latitude. (**C**) Annual Sen's slope of the climatological Chl with Mann-Kendall (MK) test significance (° $p < 0.1$, * $p < 0.05$, ** $p < 0.01$, *** $p < 0.001$) indicated. Color represents R-squared values.

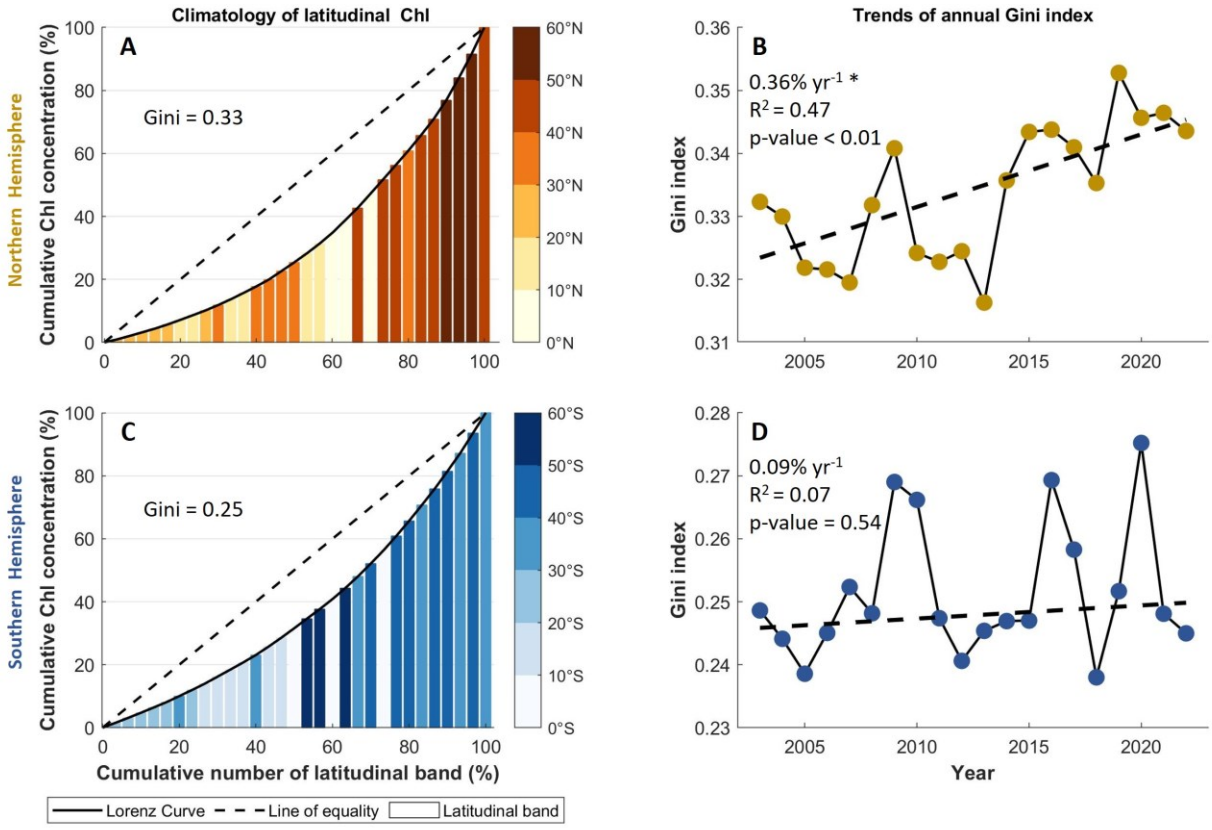

Fig. 2. Latitudinal disparity in area-integrated surface Chl concentration. (**A**, **C**) Lorenz curves of climatological Chl area-integrated over 2° latitudinal bands in the Northern (0 – 60°N) and Southern Hemispheres (0 – 60°S) during the 2003 – 2022 period. Bars represent the cumulative percentage of surface Chl integrated over 2° latitudinal bands, ordered in ascending

contribution of Chl to the total. (**B**, **D**) Interannual variability of the Gini index from 2003 to 2022 with significant trends ($p < 0.05$) indicated by an asterisk.

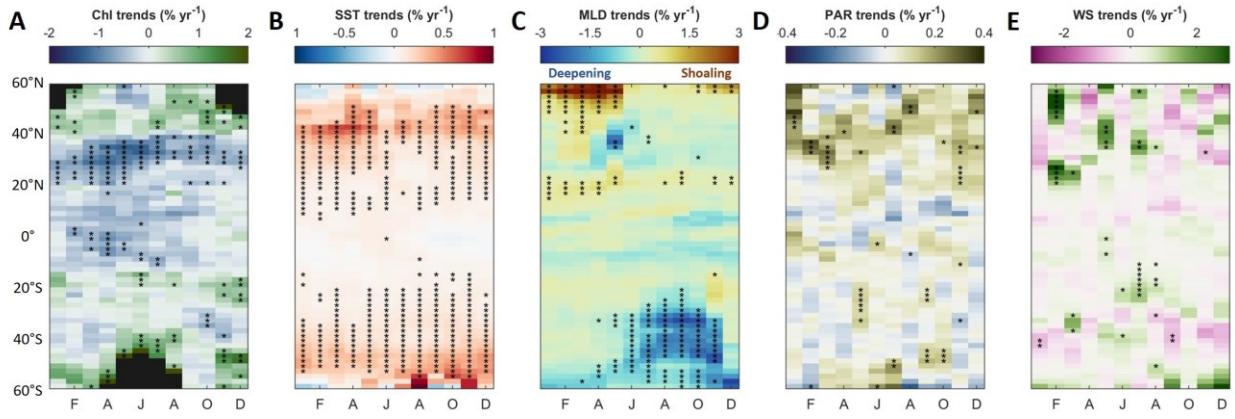

Fig. 3. Long-term trends of variables grouped by month and latitude. (A–E) Trends for Chl, SST, MLD, PAR and WS. Each grid in the panels represents an estimated slope of a linear trend of the year-to-year monthly variable at that particular latitudinal band. Asterisk indicates grids with significant trend. Black grids indicate regions where no data is available.

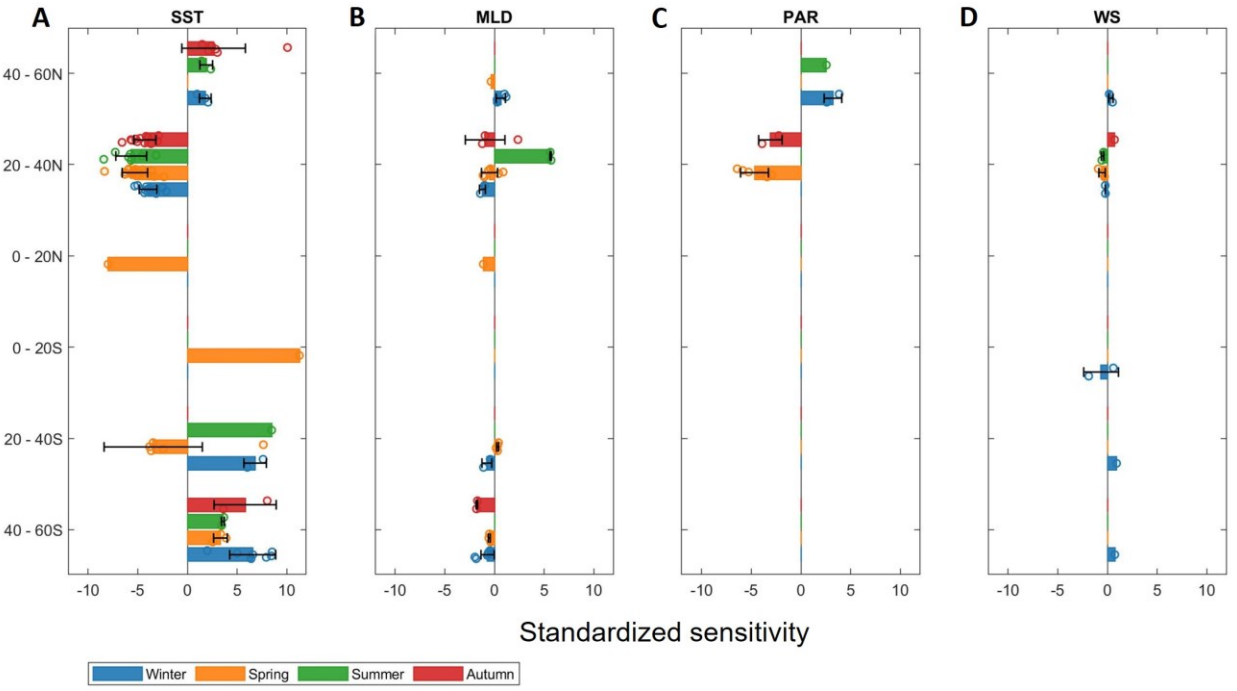

Fig. 4. Observed sensitivity of Chl to driving factors. (**A**) SST, (**B**) MLD, (**C**) PAR, and (**D**) WS. Circles represent the standardized observed sensitivity (Methods) of grids with concurrent

significant trends of Chl and driving factors. Bars represent the median observed sensitivity of grids grouped in the same season and particular latitudinal band.

5